



Compaction bands in Tuffeau de Maastricht: insights from X-ray tomography and multiscale modeling

Huanran Wu¹ · Athanasios Papazoglou² · Gioacchino Viggiani² · Christophe Dano² · Jidong Zhao¹

Received: 22 August 2019 / Accepted: 26 November 2019 / Published online: 14 December 2019
© Springer-Verlag GmbH Germany, part of Springer Nature 2019

Abstract

We present a study on compaction band in a high-porosity limestone (Tuffeau de Maastricht) based on comparison and analysis of X-ray tomography observations and computational multiscale simulations. We employ a hierarchical multiscale approach coupling the finite element method (FEM) with the discrete element method (DEM) to simulate the formation of compaction bands in Tuffeau de Maastricht. A high-porosity RVE is prepared according to X-ray tomography observations of material microstructure, and its grain-scale parameters are calibrated by data from laboratory isotropic compression and triaxial compression tests. Triaxial compression tests are simulated by FEM as a boundary value problem to observe compaction bands. The generated RVE is embedded into each integration point of the FE mesh, receiving displacement gradient as DEM boundary conditions, and is solved accordingly to produce the required mechanical responses for FEM computation without assuming phenomenological constitutive relations. The simulated global mechanical responses of the triaxial tests are found to show qualitative agreement with the experimental data. The evolution of compaction band patterns in the simulation matches remarkably well with the experimental observations in terms of fields of porosity and incremental strains. Both show two compaction fronts initiating from the two ends of the specimen and propagating toward the middle. By virtue of the multiscale approach, useful microstructural information is further extracted from the simulations to offer cross-scale insights into compaction bands. The study confirms that significant debonding accompanied by collapse of macropores and grain rearrangements is the major microstructural mechanisms causing the formation of compaction bands in high-porosity Tuffeau de Maastricht.

Keywords Compaction band · FEM × DEM · Limestone · Multiscale modeling · X-ray tomography

1 Introduction

Field observations of compaction bands in high-porosity sandstones have triggered great interest for the community of geosciences and geomechanics [4, 35]. High-porosity rocks are key hosts worldwide for hydrocarbon extraction, CO₂ sequestration and underground hazardous waste disposal. The formation of compaction bands in these rocks may cause substantial reduction in both porosity and permeability [20, 21] and lead to adverse changes to the fluid

flow related to fluid injection, storage and extraction that are highly relevant to these applications [30, 39]. There have been various laboratory experiments conducted on high-porosity rocks, particularly sandstones and limestones, to investigate the mechanisms and conditions of compaction bands during the brittle–ductile transition with the increase in mean stress [5, 6, 10, 19, 38, 49, 54]. Relevant theoretical studies have commonly considered compaction band as an end member of the complete kinematic spectrum of deformation bands [22]. Bifurcation theory has been used to predict the onset and orientation of a compaction band [8, 9, 37, 43, 44, 56]. Complex constitutive models have been developed to describe the mechanical behavior of these rocks [13, 50], along with their implementation by the finite element method (FEM) to predict and model compaction bands in boundary value problems (BVPs) [14, 15, 36]. Micromechanics-based approaches

✉ Jidong Zhao
jzhao@ust.hk

¹ Hong Kong University of Science and Technology, Clearwater Bay, Kowloon, Hong Kong

² Univ. Grenoble Alpes, CNRS, Grenoble INP, 3SR, 38000 Grenoble, France

such as the discrete element method (DEM) have also been employed to investigate the role of grain crushing and pore collapses in the formation of compaction bands [16, 34, 52].

The aforementioned progresses help to advance our fundamental understanding of compaction bands in porous rocks. However, it remains poorly understood what the key microstructural mechanisms are and how they work in triggering and changing the conditions for the development of compaction bands in high-porosity rocks. A predictive tool that enables bridging micromechanical observations with macroscopic phenomena such as compaction bands proves to be useful and indeed necessary. To this end, a coupled FEM×DEM multiscale approach based on that developed by [24] for granular media has been extended by the authors to simulate compaction bands in various BVPs for sandstones [57–60]. In this approach, a typical BVP is solved by FEM and the required constitutive response of the material is derived through direct DEM computations on the representative volume element (RVE) attached to each Gauss point of the FE mesh. This scheme helps to bypass the necessity of phenomenological constitutive models in conventional FEM and facilitates direct cross-scale analyses by linking the macroscale phenomenon (e.g., compaction bands) with its underlying microstructural mechanisms. Our early studies have identified that debonding and pore collapses can be dominant mechanisms in the absence of particle crushing. However, these studies remain simplified by the two-dimensional (2D) nature of the assumed RVE and the simulated BVPs. To advance this line of research, we extend our previous 2D studies on compaction bands to the three-dimensional (3D) scenario [26].

Tuffeau de Maastricht, a high-porosity limestone wherein compaction bands were observed, is adopted as the target material in generating our RVE. The microstructure of Tuffeau de Maastricht is investigated through high-resolution X-ray tomography to offer a comparison basis of the RVE. The micro-parameters of the RVE are calibrated based on the physical and mechanical data obtained from the experiments. A full 3D multiscale simulation is then performed to reproduce the compaction bands for comparison and validation with the experimental observations. Microscale information linking underlying mechanisms to compaction bands that cannot be directly measured in experiments, such as the particle-scale failure process, the evolution of interparticle contact forces and contact network, is further extracted from the multiscale simulation to provide a fresh, multiscale perspective to advance the understanding of compaction bands. Notably, an elastoplastic constitutive model has been developed and calibrated based on the same set of experimental data before being implemented into FEM to capture the pressure-

dependent inclination of deformation bands and their evolution with increased axial strain [47].

2 Experimental and numerical model setups

Tuffeau de Maastricht (Maastricht limestone) is a high-porosity (up to 52%) bioclastic limestone of the Upper Cretaceous period [11, 42]. It is homogeneous with rarely observed layers and consists of weakly cemented grains. The average grain size is around 0.1–0.2 mm with identifiable big inclusions and fossils. Given its high porosity and weak cementation, it is considered to be a soft rock with low strength. Compaction bands have been observed in the transitional regime from brittle to ductile failure of this limestone [7, 40, 41]. The homogeneity of the material and the likely occurrence of compaction bands make Tuffeau de Maastricht an excellent candidate for a comparative study with multiscale simulations and experimental tests under realistic 3D conditions.

2.1 Triaxial compression tests with X-ray tomography

A comprehensive set of laboratory experiments have been conducted at *Laboratoire 3SR* to study the mechanical behavior of Tuffeau de Maastricht. The formation and development of compaction bands in triaxial compression tests have been examined with X-ray tomography [40, 41]. The triaxial compression tests were performed on dry cylindrical specimens 10 mm in diameter and 20 mm in height (see Fig. 3a) under confining pressures ranging from 0 to 5 MPa. The specimens are deformed ‘in-situ’ (i.e., inside an X-ray tomography machine), allowing multiple

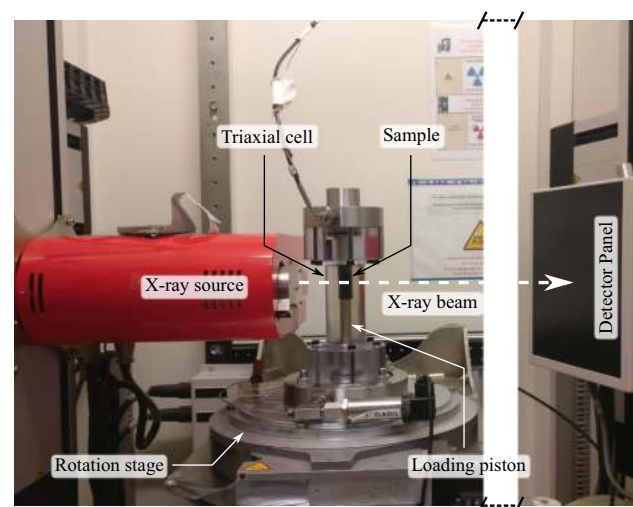


Fig. 1 Setup of the triaxial compression experiments with in-situ X-ray scanner at *Laboratoire 3SR*

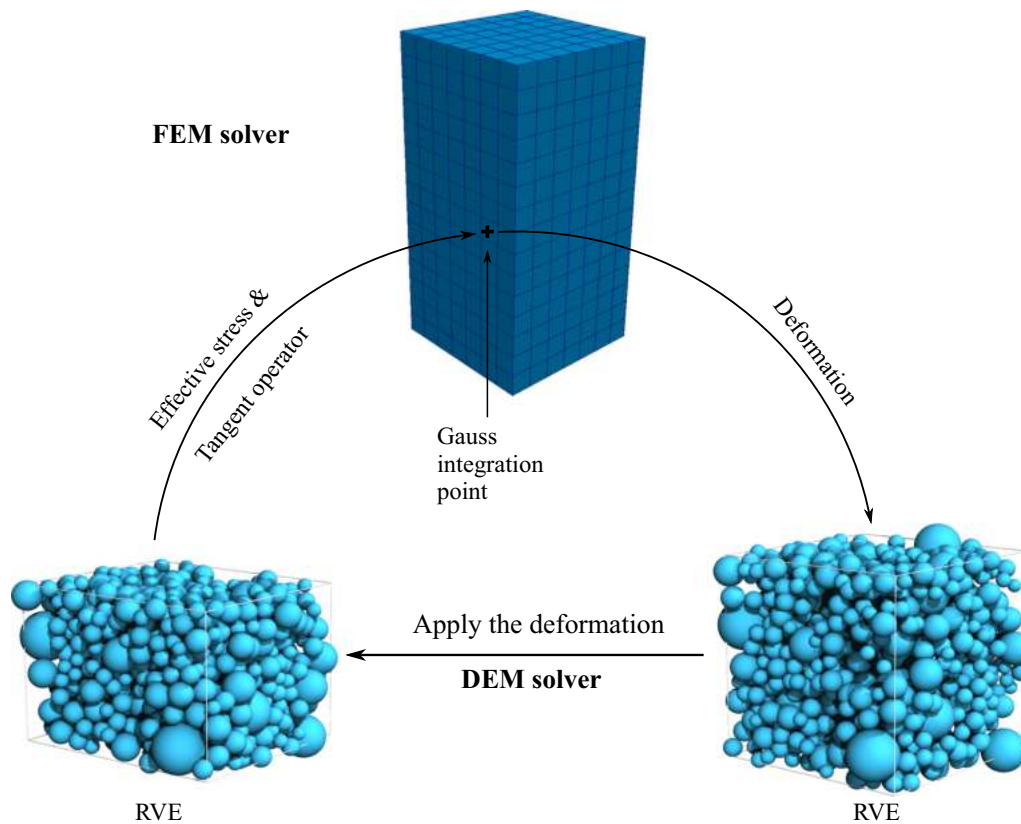


Fig. 2 The coupled FEM×DEM scheme for 3D hierarchical multiscale modeling of granular rocks

states to be imaged in 3D [2, 40] (see the experimental setup in Fig. 1). Technical details of the X-ray scanner at 3SR can be found in [1, 51].

2.2 3D hierarchical multiscale modeling

Based on the physical and mechanical data obtained in the experiments on Tuffeau de Maastricht, a 3D hierarchical multiscale simulation is performed. The multiscale scheme adopts FEM to solve a BVP and the DEM to feed the required constitutive material responses at each Gauss point of the FE mesh. The FEM solver (using the open-source code *Escript* [45]) passes the local deformation to the RVE attached at each Gaussian point, and the DEM solver (based on the open-source code *Yade* [48]) is used to solve the RVE packing at the applied deformation and to return the stresses and tangent operator back to the FEM solver (see Fig. 2). The interested reader is referred to [26] for technical details about the formulation and solution procedure. We note, however, that the current scheme is based on a first-order homogenization formulation without any regularization, which results in mesh dependency of the solutions. To resolve this issue, one needs to resort to second-order homogenization scheme and/or advanced regularization techniques, such as nonlocal or second

gradient theories [12, 18, 31]. Nevertheless, the adoption of high-order elements in conjunction with reasonable fine mesh has been found helpful to reasonably mitigate mesh dependency and achieve acceptable consistencies and convergence in terms of global responses and occurrence of different deformation band patterns [27, 61]. Relevant discussions of this multiscale method concerning its computational performance, mesh dependency and possible engineering applications can also be found in [3, 17, 18, 27–29, 33, 46, 53, 62].

2.3 RVE preparation for Tuffeau de Maastricht

X-ray tomography at 1 μm resolution provides a clear picture of the grain-scale microstructure of Tuffeau de Maastricht (see Figs. 3b–c). Quite large pores are observed clearly among the intergranular voids (in dark in the images). Critical for the hierarchical multiscale modeling to reproduce the material responses of Tuffeau de Maastricht is to prepare an RVE that mimics the observed microstructure. A 3D high-porosity RVE is prepared by a particle-removing technique similar to that suggested by [59]: (a) A suitable packing of spherical particles with a grain size distribution similar to real material is generated; (b) the packing is isotropically compressed to a desirable

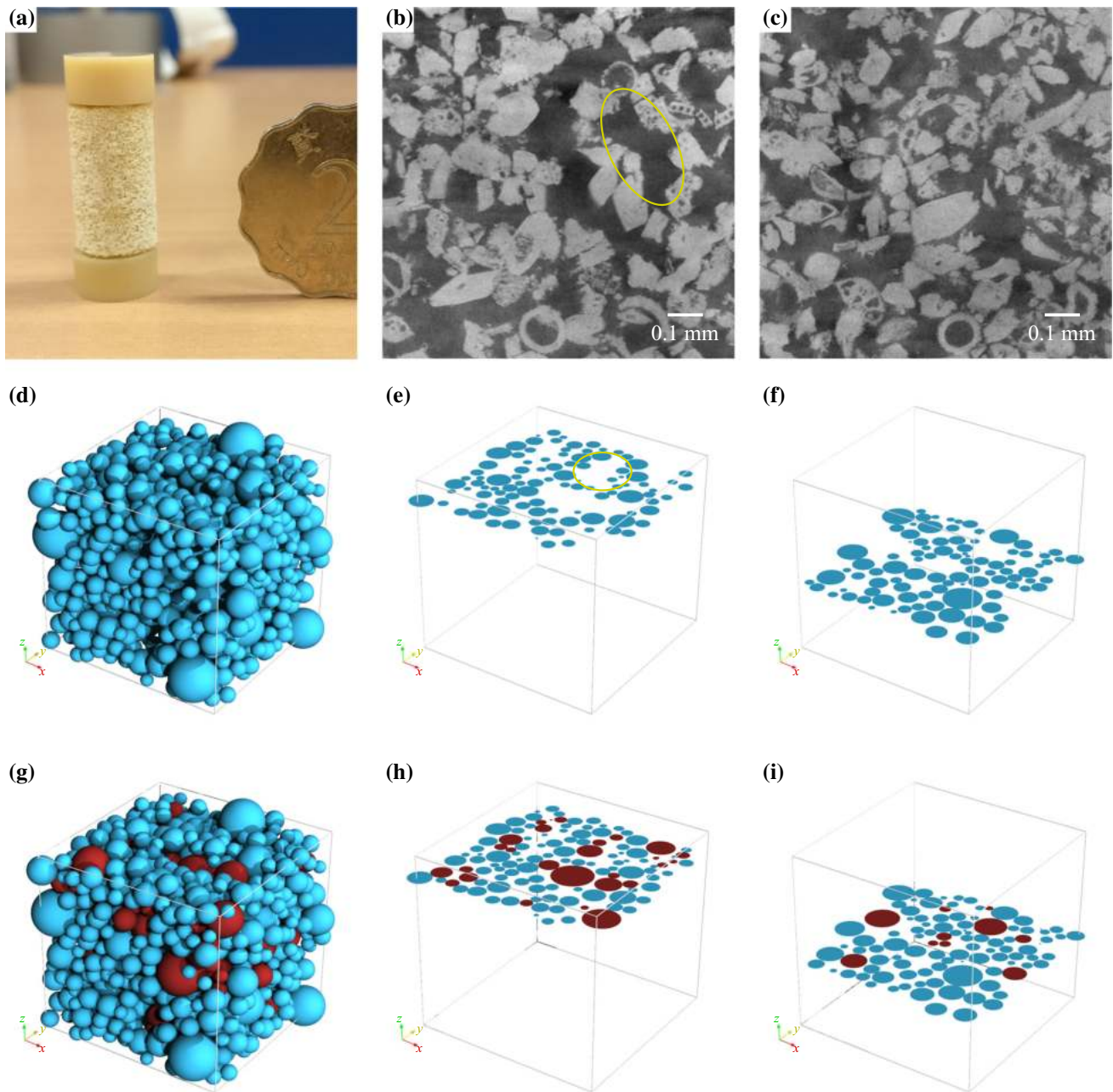


Fig. 3 Microstructures of **a–c** the real specimen (porosity 0.499, grains in light, voids in dark), **d–f** the high-porosity RVE (porosity 0.516) and **g–i** the RVE before particle removal (porosity 0.396, the particles to be removed are in red) (colour figure online)

target confining pressure (e.g., 90% of the initial pressure in the triaxial tests) with large frictional coefficient to produce a loose packing; (c) interparticle contacts of the packing are assigned with appropriate values of cohesion to mimic the natural cementation; (d) a random portion of particles are removed from the packing to reproduce macropores observed in Tuffeau de Maastricht and similar porosity; (e) the packing is further isotropically compressed to the targeted confining pressure in the experimental tests. The microstructure of the generated RVE is

presented in Fig. 3d. 2D sections of the RVE are compared in Fig. 3e–f with those from the real specimen. The microstructure of the RVE before particles removal is shown in Fig. 3g–i for reference with the removed particles in red. Notably, the macropores formed in the high-porosity RVE via particle removal (see the yellow circle in Fig. 3e) share reasonable similarities with the macropores in the real specimen (see Fig. 3b).

At each contact, interparticle cohesion is applied before particle removal to maintain the particles in place. Herein,

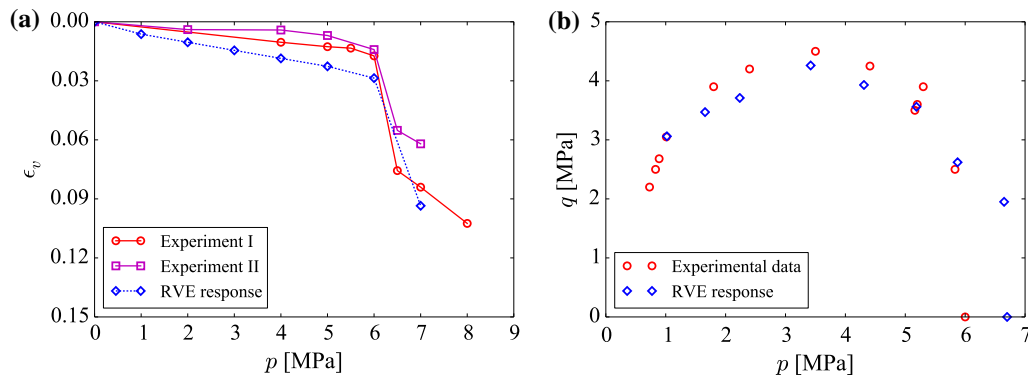


Fig. 4 Comparison between the RVE responses and the experimental data in terms of **a** volumetric strain (ϵ_v) versus mean stress (p) in isotropic compression tests and **b** failure surface in the deviatoric stress (q) versus mean stress (p) plane. Note that the volumetric strain ($\epsilon_v = (n_0 - n)/(1 - n)$, where n is the global porosity of the specimen, and n_0 is its initial value) was determined based on 3D images in the experiments

the interparticle contact behavior is described by a bonded contact model consisting of a linear force–displacement contact law, a Coulomb-type friction and thresholds for tensile and shear forces at a contact. The normal and tangential contact stiffnesses are defined as:

$$k_n = E_c r^* \tag{1}$$

$$k_t = \nu_c k_n \tag{2}$$

where $r^* = \frac{2r_1 r_2}{r_1 + r_2}$, and r_1 and r_2 are the radii of the two particles in contact. The thresholds for tensile and shear forces are determined as follows:

$$F_n^{\max} = c \min(r_1, r_2)^2 \tag{3}$$

$$F_t^{\max} = c \min(r_1, r_2)^2 + F_n \tan \phi \tag{4}$$

where c is the cohesion strength and ϕ is the interparticle friction angle. If either of the thresholds is exceeded, the interparticle bond is eliminated leaving a pure frictional contact (i.e., $F_t \leq F_n \tan \phi$).

The micro-parameters for the RVE are determined based on the experimental data. The radii of the particles follow a grain size distribution similar to the real material (particles with radii smaller than 0.08 mm are neglected). The density of the particles is scaled 100 times with respect to the real material to speed up the DEM computation in attaining quasi-static convergence for each step, a commonly adopted technique in DEM modeling [26, 32]. The other parameters are calibrated based on the mechanical data obtained from the triaxial and isotropic compression tests. Specifically, c is calibrated to be the largest value at a comparable volume reduction when the confining pressure increases from 6 to 7 MPa in isotropic compression. E_c and ν_c are calibrated as a compromise between the elastic responses in isotropic and triaxial compression (see Figs. 4a, 5a). The values adopted for the micro-parameters of the RVE are as summarized in Table 1.

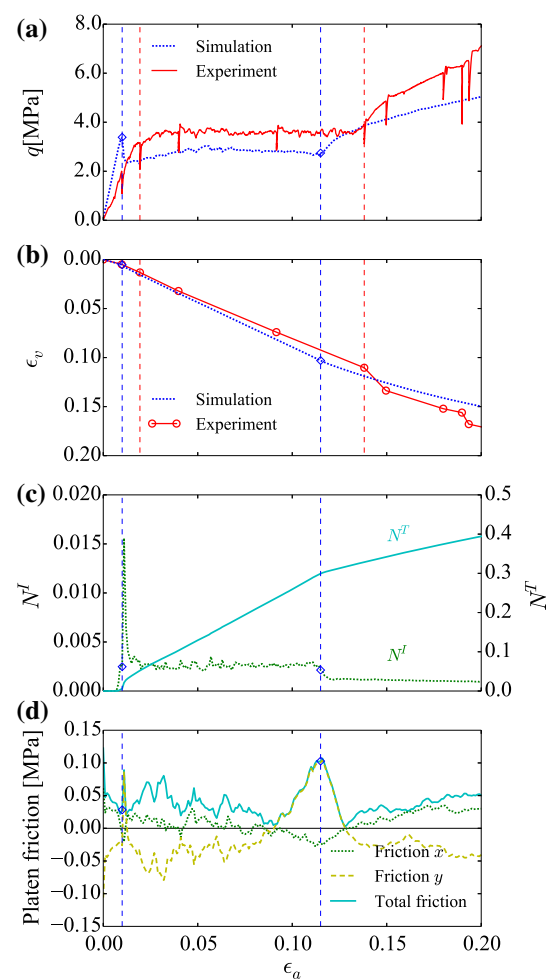


Fig. 5 Global responses of the multiscale simulation in terms of **a** deviatoric stress (q), **b** volumetric strain (ϵ_v), **c** incremental (N^I) and accumulated (N^T) normalized debonding number and **d** platen friction with increased axial strain (ϵ_a). The experimental records of q and ϵ_v are plotted in **a–b** for comparison

Table 1 Calibrated micro-parameters for the high-porosity RVE representing Tuffeau de Maastricht

r (mm)	Particle density (kg/m ³)	E_c (GPa)	ν_c	ϕ (°)	c (MPa)
0.8–3.15	2.47×10^5	4	0.5	20	68.6

A comparison between the RVE behaviors and the experimental responses is presented in Fig. 4. The failure surface in the deviatoric stress ($q = \sigma_1 - \sigma_3$, where σ_1 and σ_3 are the major and the minor principal stresses, respectively) versus mean stress ($p = (\sigma_1 + 2\sigma_3)/3$) plane is obtained based on the critical stress states, beyond which an accelerated increase in volumetric strain ('shear-enhanced compaction') is observed under triaxial compression as compared to the isotropic compression condition [55]. Notably, the prepared RVE produces largely comparable, but slightly softer response upon isotropic compression (Fig. 4a). The failure surface obtained from the simulations matches reasonably well with the corresponding surface obtained from the actual experiments (Fig. 4b).

3 Compaction bands in triaxial compression: experiments versus multiscale simulations

Under a confining pressure of 4 MPa, compaction bands were observed in the laboratory triaxial compression tests initiating from the two ends of the specimen and propagating toward the middle with increasing axial strain. A multiscale triaxial simulation with a prismatic specimen (10 mm × 10 mm × 20 mm) under the same confinement is conducted to validate the prepared RVE. The top and bottom surfaces are assumed rough (no horizontal displacement) to achieve a converged solution. The specimen is discretized into 735 (7 × 7 × 15) 20-node hexahedral elements (see Fig. 2). A reduced integration with 8 Gauss integration points for each element is adopted to reduce the computational cost (see also in [26]). With 1033 particles for every RVE, the total number of particles involved amounts to over 6 million. Through parallel computing (see details in [24]), a typical simulation in this study (ε_a to 20% with 200 quasi-static loading steps) costs about 320 h on a local server with 2 × 10-core 3.0 GHz CPU (Intel Xeon CPU E5-2690 v2) and 64 GB RAM. As a simulation involving millions of discrete particles, the multiscale approach with efficient parallelization is more efficient than pure DEM simulations.

3.1 Global responses

The global responses of the simulation in terms of the deviatoric stress (q), the global volumetric strain (ε_v), the global normalized debonding number (both incremental

value N^I and accumulated value N^T) and the platen frictional resistance (horizontal stress on the top boundary) are presented in Fig. 5. The experimental data for q and ε_v are plotted in Figs. 5a, b for comparison. Note that the debonding number and platen frictional resistance are not available from experimental tests. Reasonable agreements are observed between the simulation results and the experimental data. In particular, three similar stages could be identified clearly from the stress–strain relation in both the experiment and the simulation. Two dashed vertical lines (blue for the simulation and red for the experiment) are used to divide the entire process into (1) pre-failure stage, (2) plateau stage and (3) re-hardening stage. The increase in ε_v is approximately linear, with a slightly higher increasing rate noticed at the plateau stage than at the pre-failure stage.

Despite the great similarities observed between simulations and experiments, some discrepancies do exist. Unlike the gradual transition from pre-failure stage to plateau stage, a higher peak followed by a sudden stress drop is observed in the multiscale simulation, which leads to a lower stress plateau relative to the experimental data. The simulation also displays a softer behavior than the experiment at the re-hardening stage. Moreover, the increasing rate of ε_v for the re-hardening stage is smaller than that for plateau stage in the simulation, while a larger increasing rate is observed at the re-hardening stage in the experiment.

The evolution of interparticle debonding is plotted in Fig. 5c to illustrate the damage process. An apparent peak for the incremental normalized debonding number (N^I) is observed at the beginning of the plateau stage, which corresponds to the initiation of compaction bands. N^I is then essentially constant during the subsequent plateau stage. N^I decreases at the transition to the re-hardening stage and attains a lower plateau afterward. Consequently, the accumulated normalized debonding number (N^T) displays an interesting piecewise linear trend. The increasing rate of N^T at the re-hardening stage is smaller than that at the plateau stage. Notably, the value of N^T is around 0.3 at the end of the plateau stage, indicating that a large portion of interparticle bonds persist.

Since rough boundaries with no lateral displacement are adopted in the simulation for the top and the bottom boundaries, there are frictional reaction stresses between the loading platen and the specimen (horizontal stresses on the top boundary) which are presented in Fig. 5d. The total

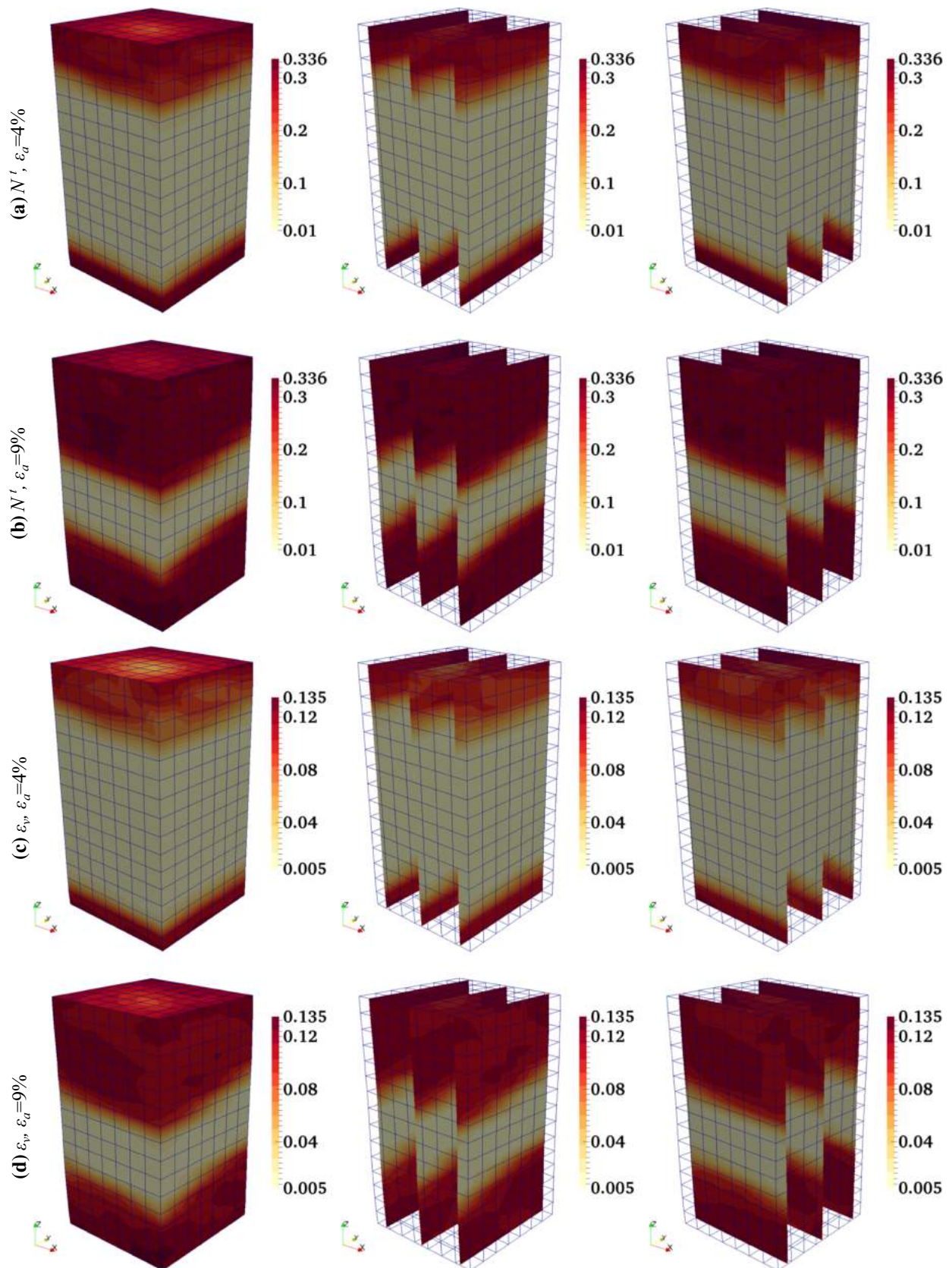


Fig. 6 Contours displaying the evolution of compaction bands in terms of **a–b** the local accumulated normalized debonding number (N') and **c–d** the local volumetric strain (ϵ_v)

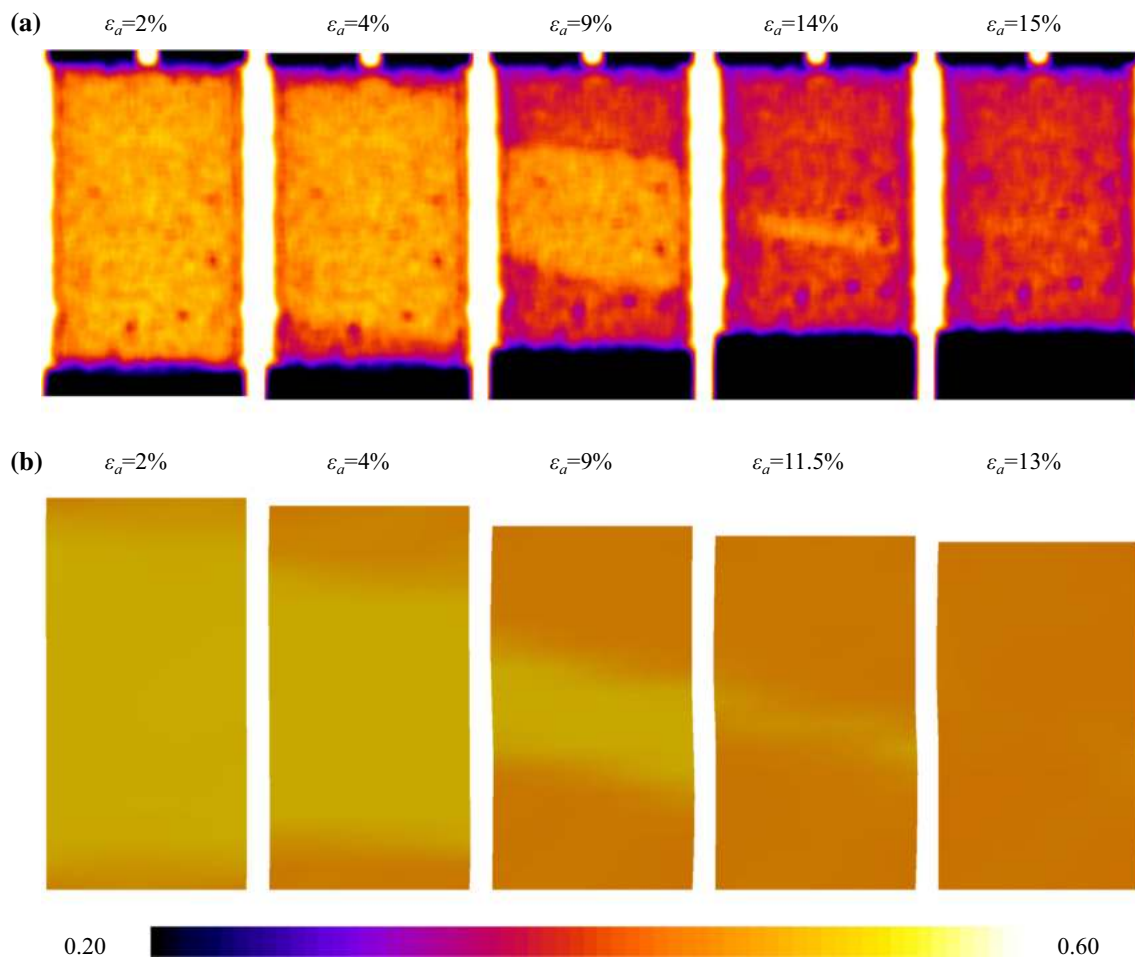


Fig. 7 2D slices of porosity field at different axial strains (ε_a) **a** in the experiment [40] and **b** in the simulation

frictional reaction stress is usually small (as compared to the confining pressure and deviatoric stress) whose peak appears at the beginning of the plateau stage and re-hardening stage. The friction along the y direction is generally larger than that along the x direction. Coincidentally, the tilting angle of the compaction fronts along the y direction is larger than that along the x direction as well (see Fig. 6).

3.2 Macroscale localization patterns

It is interesting to compare the localization patterns in the multiscale simulation with those in the experiment. Figure 6 presents the evolution of compaction bands obtained from the multiscale simulation, in terms of contours of local accumulated normalized debonding number (N^l) and local accumulated volumetric strain ($\varepsilon_v = \text{tr}\boldsymbol{\varepsilon}$, where $\boldsymbol{\varepsilon}$ is the strain tensor and ‘tr’ stands for the trace of a tensor). Contours of both variables demonstrate rather consistent patterns of compaction bands, initiating from the top and bottom boundaries and propagating gradually toward the middle of the specimen along the z direction. The

compaction fronts (the boundaries between the compacted and the uncompacted zones) are roughly horizontal at $\varepsilon_a = 4\%$. However, they become slightly tilted as ε_a increases to 9%. The 3D contours and the 2D slices indicate that the fronts are almost horizontal along the x direction and tilt at an angle of around 10° along the y direction.

Combined techniques of in situ X-ray tomography and 3D Digital Image Correlation (DIC) have enabled the initiation and the development of compaction bands, in terms of porosity and incremental strains, in the triaxial experiments to be fully recorded and identified [40, 41]. 2D sections of the specimen displaying compaction bands of the largest tilting angle (perpendicular to the x direction) are selected to make one-to-one comparisons as follows.

Porosity field The slices of porosity field in the experiment and in the simulation at different axial strains are compared in Fig. 7. Despite the slightly larger initial porosity of the RVE in the simulation (0.516) than that of the specimen in the experiment (0.499), the evolution of the porosity field in the simulation is almost identical to the

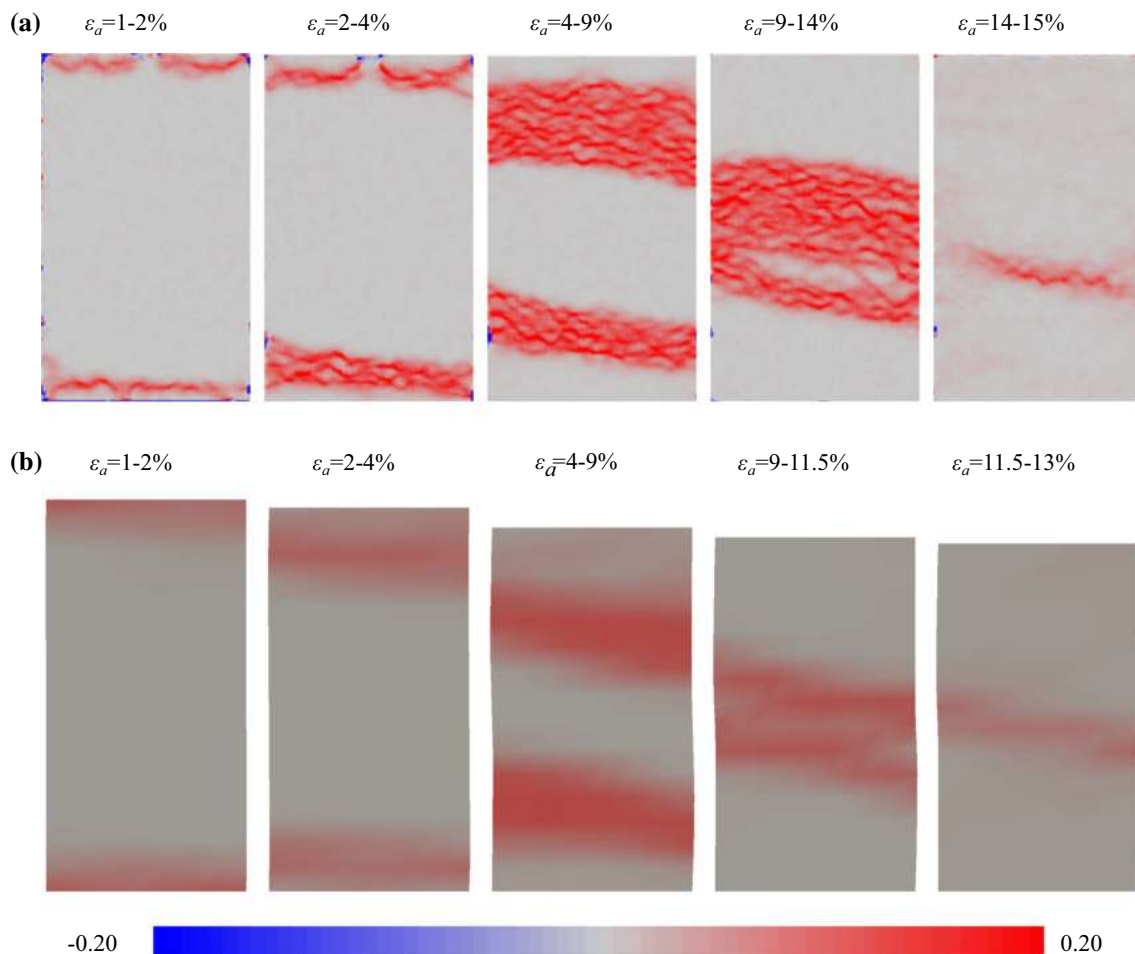


Fig. 8 2D slices of incremental volumetric strain at different increments of axial strain (ε_a) **a** in the experiment and **b** in the simulation

one observed in the experiments. As the axial strain increases, two localized compacted regions with reduced porosity form near the top and the bottom ends of the specimen. The compacted regions gradually propagate toward the middle of the specimen and finally meet each other. Then the entire specimen is further compacted to a relatively homogeneous state with a porosity around 0.4. Note that the full compaction of the specimen appears at $\varepsilon_a = 15\%$ in the experiment and at $\varepsilon_a = 13\%$ in the simulation, respectively. Nevertheless, the re-hardening stage identified from the stress–strain relation starts from $\varepsilon_a = 13.2\%$ in the experiment and from $\varepsilon_a = 11.5\%$ in the simulation. This suggests that re-hardening starts before the entire specimen is compacted.

Incremental strain field 3D DIC has been performed in the experiments to obtain the strain field in the specimens. The slices of incremental volumetric strain (ε_v) and incremental deviatoric strain ($\varepsilon_q = \sqrt{\frac{2}{3}} \text{dev} \boldsymbol{\varepsilon} : \text{dev} \boldsymbol{\varepsilon}$, where ‘dev’ takes the deviator of a tensor and ‘:’ denotes the double contraction operator) in the experiment and the multiscale simulation at different increments of axial strain

(ε_a) are plotted in Figs. 8 and 9 to demonstrate the evolution of compaction bands. Note that the increments of axial strain for the last two figures in each set are different (9–14% and 14–15% for the experiment; 9–11.5% and 11.5–13% for the simulation) to capture the final end of the compaction. Subtle differences within the compacted regions are distinguishable through 3D DIC, while the simulation results appear to be more or less homogeneous within those regions. Other than that, the incremental strain fields from the simulation match amazingly well with those from the experiments. The compaction bands initiate from the top and the bottom of the specimen, and then propagate toward the middle with little or no incremental strain in the compacted region. The entire process of compaction banding including the initiation, the propagation and the final state, is well captured in the simulation.

3.3 Microscale analyses

The hierarchical multiscale approach provides the possibility of directly linking the macroscale and the microscale,

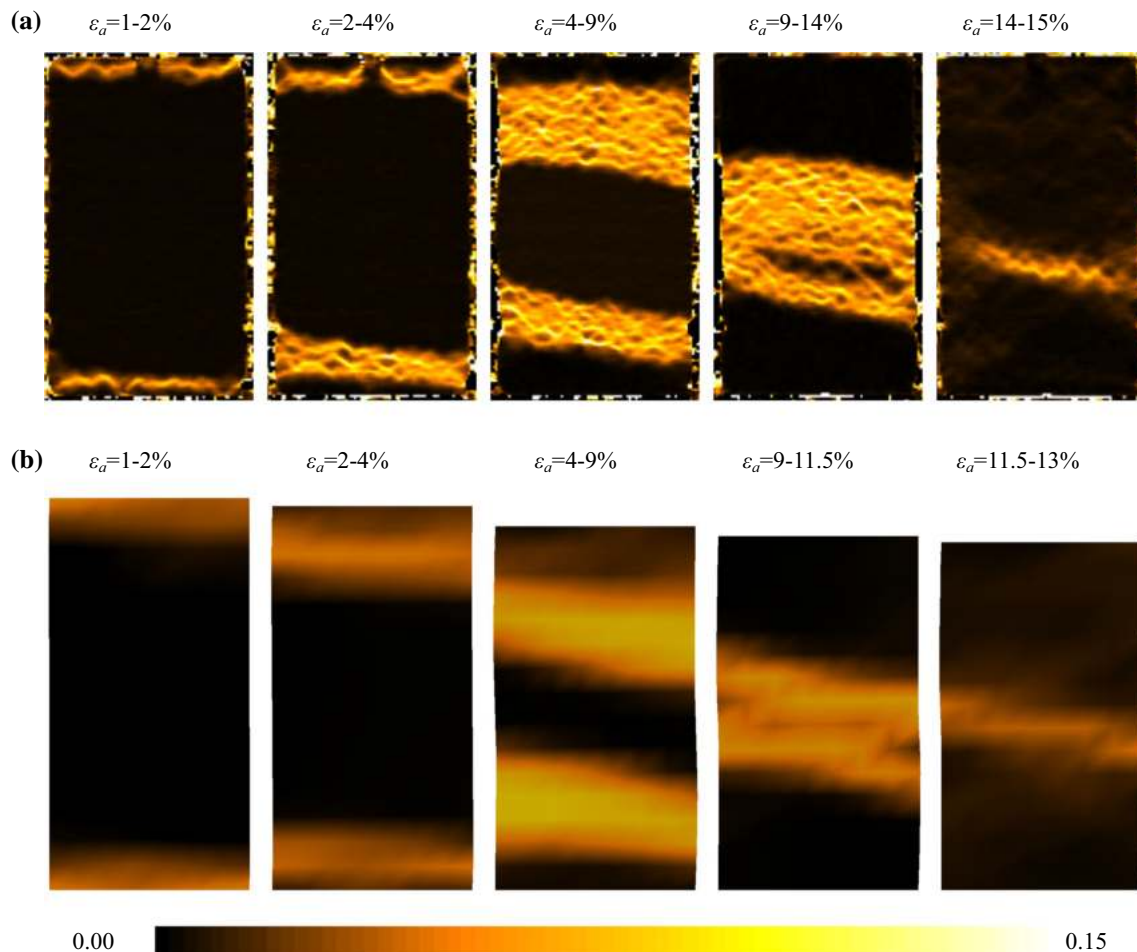


Fig. 9 2D slices of incremental deviatoric strain at different increments of axial strain (ε_a) **a** in the experiment [40] and **b** in the simulation

which facilitates cross-scale understanding of the underlying micromechanisms accounting for complex macro-scale phenomena. This advantage is taken to carry out systematic microscale analyses in the following to offer another fold of understanding on compaction bands.

3.3.1 Propagation of compaction fronts

A series of RVEs sharing the same x and y coordinates are selected to present the evolution of compaction fronts along z direction. Figure 10a–c presents the evolutions of their incremental normalized debonding number (N^i , akin to acoustic emission rate to quantify damage in experiments [10]), deviatoric stress (q) and accumulated volumetric strain (ε_v) with axial strain (ε_a), respectively. The beginning and the end of the plateau stage are marked with two blue-dashed vertical lines in Fig. 10a–c, and the intersections between the second line and the curves are marked with different symbols in Fig. 10c. The relation between ε_v and deviatoric strain (ε_q) is shown in Fig. 10d with the same markers indicating the end of the plateau

stage. The locations of the selected RVEs are marked in the inset with the corresponding markers.

The evolutions of N^i , q and ε_v with ε_a for all the RVEs show a qualitatively similar trend, despite fluctuations and variable failure sequences. The failure of the first RVE occurs at the beginning of the plateau stage, possibly affected by the rough boundary. Afterward, other RVEs fail in sequence at almost the same intervals, indicating a steady propagation of the compaction fronts. In Fig. 10b, a specific RVE is highlighted above others for better illustration. The compaction stage of this RVE is marked in Fig. 10a–c for easy comparison. The pre-compaction (a peak of q), early compaction (the peak of N^i) and post-compaction instants are marked with solid diamonds in sequence, while the others with empty ones. Following the linear increase in q in the pre-failure stage, a mild stress drop is observed at the beginning of the plateau stage due to unloading with negligible N^i . After a short plateau, q gradually builds up to a peak before the RVE fails with a quite brittle stress drop, a burst of N^i and a surging increase in ε_v . The peak of N^i emerges at the beginning of the

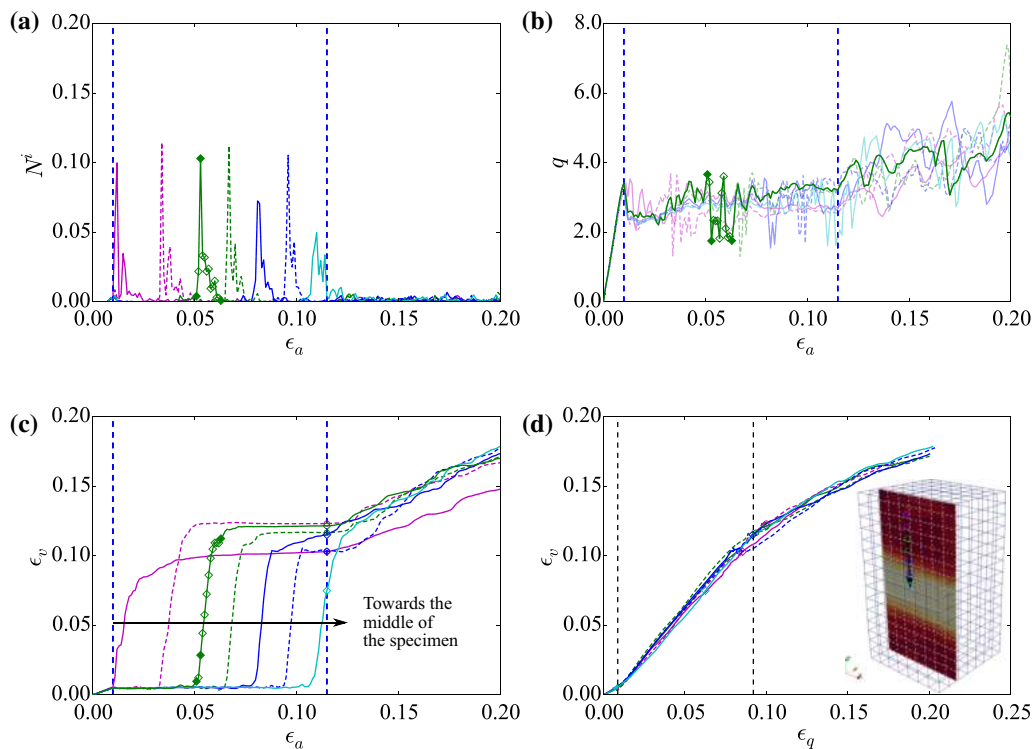


Fig. 10 Local responses of selected RVEs sharing the same x and y coordinates to present the propagation of the compaction front. The evolutions of local **a** incremental normalized debonding number (N^i), **b** deviatoric stress (q) and **c** volumetric strain (ϵ_v) with increased axial strain (ϵ_a) and **d** ϵ_v versus deviatoric strain (ϵ_q)

localized compaction, while ϵ_v increases steadily toward the end of the compaction stage. q fluctuates heavily during the compaction stage of the RVE and returns to a plateau afterward with negligible N^i and almost constant ϵ_v until the end of the plateau stage. The re-hardening stage is distinguished from the plateau stage by a build-up of q with occasional drops, a gradual increase in ϵ_v , and slight N^i as ϵ_a increases. Note that the relatively small ϵ_v of the last RVE at the end of plateau stage agrees with the previous observation that the re-hardening stage begins before the entire specimen is compacted.

Figure 10d displays qualitatively similar evolutions of ϵ_v with ϵ_q for all the RVEs as well. They show (1) a gentle linear range (corresponding to the pre-failure stage), (2) a steeper linear range (corresponding to the plateau stage) and (3) a gradually flattened range (corresponding to the re-hardening stage), separated roughly by the two black-dashed lines. The microscale strain ratio ϵ_v/ϵ_q proves to be an effective indicator to describe the transition of localization modes. The decreasing slope with the transition from the plateau stage to the re-hardening stage indicates the change in failure mode from compaction-dominated to shear-dominated.

3.3.2 Evolution of internal structure

Tuffeau de Maastricht features a high-porosity structure with the presence of macropores (see Fig. 3b–c). It is instructive to examine the change in the internal structure in relation to the initiation and development of compaction bands. Figure 11 presents a comparison of the microstructure for the highlighted RVE before (see the peak of q marked by the first solid diamond) and after (see the last solid diamond) the localized compaction in Fig. 10a–c. Visualized with translucent particles, clumps of light color representing macropores are observed in the pre-compaction packing (see Fig. 11a, c). They either reduce in size or disappear with the development of localized compaction, indicating the collapse of macropores (see Fig. 11b, d). Rather consistent observations can be found in the force chain networks as well. There are regions with rare force chains in the pre-compaction network (Fig. 13b, e) corresponding to macropores. These regions disappear in the post-compaction network due to the collapse of macropores which facilitates new contacts and new force chains (Fig. 13c, f).

The change in local porosity for this RVE may be informative for understanding the porosity reduction process during the formation of compaction bands. The local porosity is calculated based on Voronoi tessellation. The

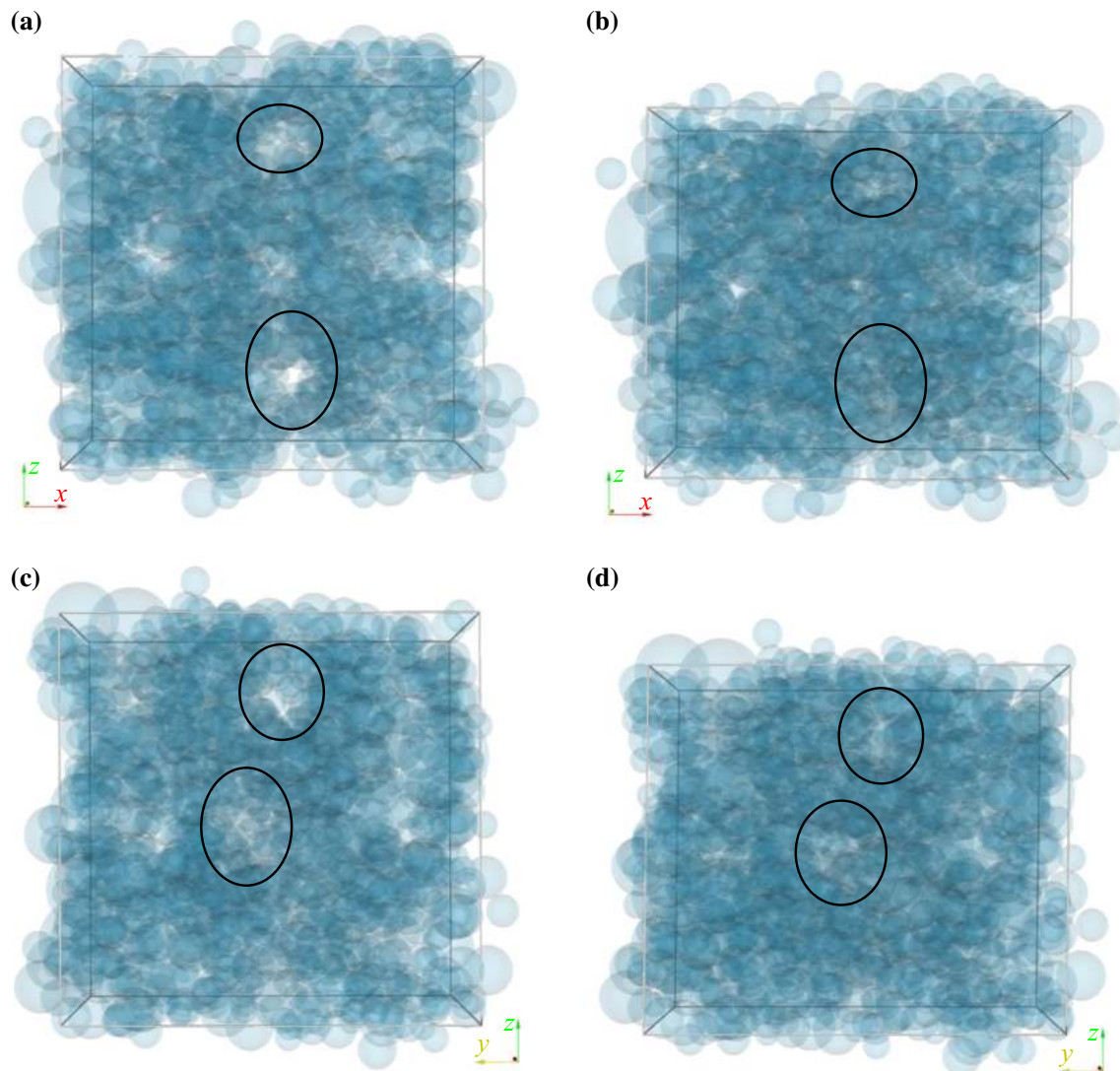


Fig. 11 Packing structures with translucent particles before (left column) and after (right column) the localized compaction along (a–b) the $+y$ and (c–d) the $+x$ view directions

distributions for the packing before particle removal (porosity 0.396, see Fig. 3g–i), the initial high-porosity packing (porosity 0.516, see Fig. 3d–f), the packing at early compaction stage (porosity 0.501, see the middle solid diamond in Fig. 10a–c) and the post-compaction packing (porosity 0.458, see the last solid diamond in Fig. 10a–c) are plotted in Fig. 12a. Notably, the local porosity in the pre-removal packing presents a normal distribution or k -Gamma distribution (see [25]). The high-porosity packing has been prepared by removing some random particles, resulting in rightward shifting of the local porosity distribution as compared to the pre-removal packing. Prior to the occurrence of localized compaction, the structures of the two packings remain roughly the same (not presented here). The internal structure transforms considerably during the compaction stage of the RVE,

since the localized compaction starts with a surging of debonding events. The local porosity changes for each particle (as compared to the initial high-porosity packing) at the inception and toward the end of the compaction are presented in groups based on its initial local porosity as box plot in Fig. 12b. The short lines inside the box and the solid markers indicate the median values and the mean values, respectively, and they present the general trend of the specific group. The packing at the early compaction stage shows a mild scatter with a gentle decrease in the high-porosity (>0.6) portion. The scatter is associated with the particle rearrangements, while the porosity reduction in the high-porosity portion pertains to the collapse of macropores. As the compaction progresses steadily, the packing at the end of compaction shows an increased scattering feature with a substantial reduction in the high-porosity

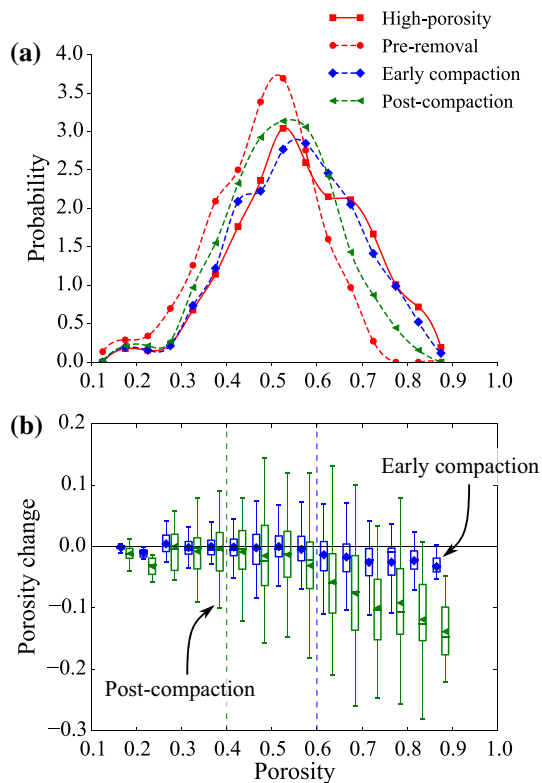


Fig. 12 **a** Comparison of the local porosity distribution among the packing before particle removal, the initial high-porosity packing, the packing at the early compaction stage and the post-compaction packing. **b** Porosity change for each particle in box plot (grouped based on initial local porosity) for the packings at the early and the end of compaction stage as compared to the initial high-porosity packing. Solid markers indicate the mean values

portion. Moreover, a positive correlation between the initial porosity and the reduction of porosity is observed for porosity greater than 0.4, suggesting a dominance of collapse of macropores over the porosity reduction. Consequently, the local porosity distribution curve shifts leftward from its initial position for the high-porosity packing. Interestingly, the peak probability porosity for pre- and post-compaction packings does not shift, indicating the dominant sizes of pores do not change much during the compaction. The curve for the post-compaction packing is in between of that for the pre-removal packing and the initial high-porosity one. Therefore, the compaction process is accompanied by grain rearrangements, collapse of macropores and induced porosity reduction that tends to transform a high-porosity packing to the pre-removal state.

Figure 13 further illustrates the evolution of force chain network of the initial high-porosity packing through the pre-compaction state (see the first solid diamond in Fig. 10a–c) to the post-compaction state (see the last solid diamond in Fig. 10a–c). Each cylinder in Fig. 13a–f connects the centers of two particles in contact with both its radius and color indicating the magnitude of the contact

normal force (see [23]). Note that tensile contact forces ($f_n < 0$) are presented in blue in the figure. Given the presence of both tensile and compressive contact forces, a spherical histogram is presented in Fig. 13g–i to characterize the evolution of contact-based anisotropy—adapted from [63]. Each bar in the histogram represents a normalized local average contact normal force $\bar{f}_n / \langle \bar{f}_n \rangle$ in that direction, where \bar{f}_n is the average magnitude of the normal forces falling in that direction range and $\langle \bar{f}_n \rangle$ is the average of \bar{f}_n over all bars. A packing with isotropically distributed normal forces will yield a sphere with radius of 1. Despite the macropores (regions with rare force chains, see Fig. 13a, d), the initial high-porosity packing is largely isotropic (Fig. 13g). The packing structure at the pre-compaction state remains nearly intact as compared to the initial one with the persistence of the macropores and the highly intensified contact normal forces (Fig. 13b, e). The histogram displays an elongation along z direction (Fig. 13h) indicating strong force chains formed along the loading direction, which agrees with the observation of the force chain network. The tensile forces distributing along the horizontal direction intensify the anisotropy. As the packing goes through the compaction stage, the macropores collapse and new contacts and force chains are formed at the post-compaction state (Fig. 13c, f). The packing becomes less anisotropic (Fig. 13i) as compared to its pre-compaction state, but still presents certain degree of anisotropy as compared to the initial state due to the development of deviatoric loading condition (see Fig. 10b).

4 Conclusion

A 3D multiscale study on Tuffeau de Maastricht has been conducted to investigate the initiation and the evolution of compaction bands. A high-porosity RVE has been prepared based on the experimental data obtained at *Laboratoire 3SR*, including the microstructure observed from 3D tomography, and the mechanical responses in isotropic and triaxial compression. Triaxial compression has been simulated by incorporating the prepared RVE into a coupled FEM×DEM multiscale modeling approach. The development of compaction bands in the multiscale simulations has been compared with the experimental observations. Key findings from this study are summarized as follows:

1. The high-porosity RVE, which contains macropores resembling those in the real material, could produce similar mechanical responses as observed in the experiments, including failure surface and volume reduction under isotropic compression.
2. Patterns of compaction band in multiscale simulations of triaxial compression of the high-porosity specimen

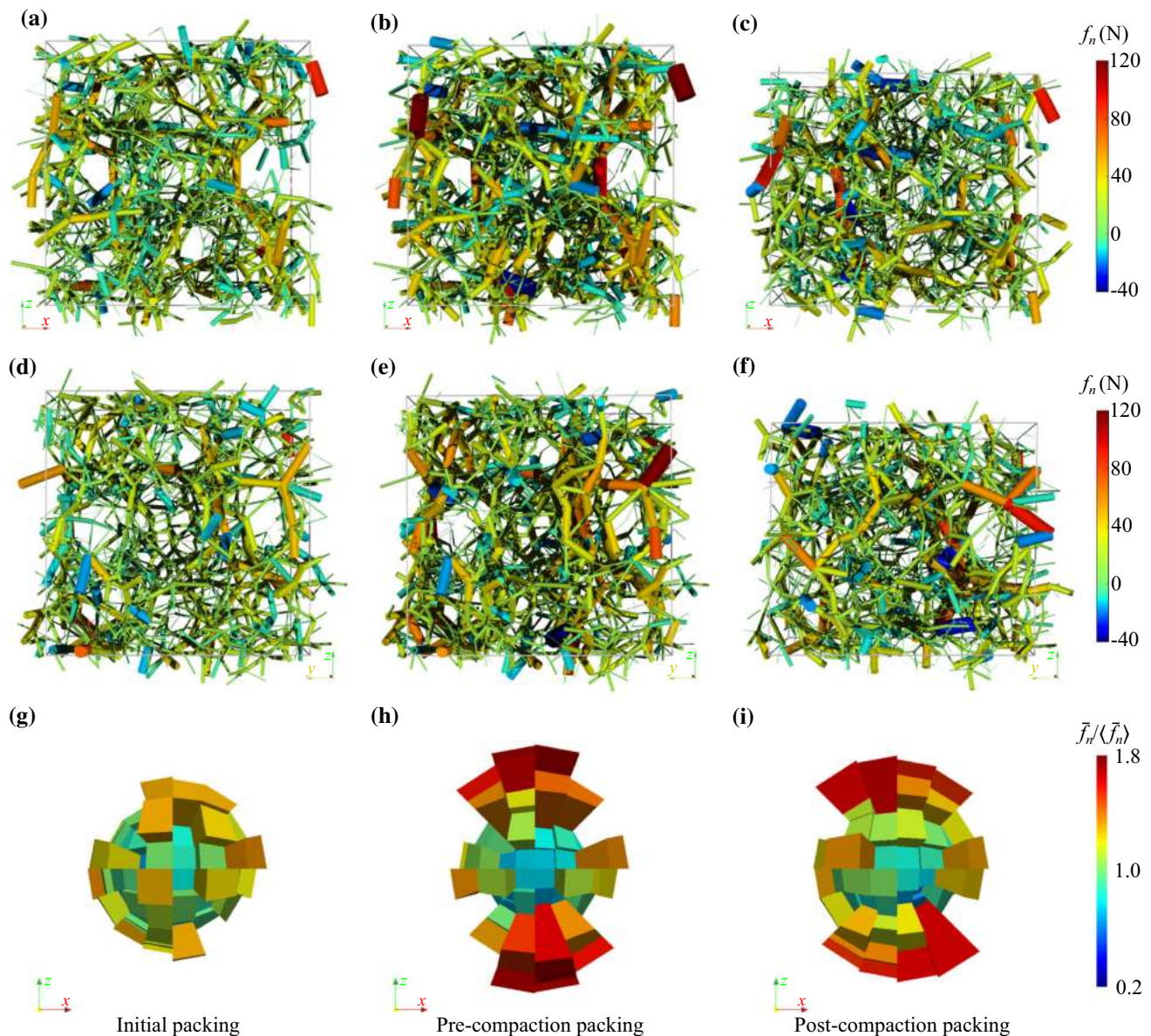


Fig. 13 Force chain networks and 3D histograms of local average contact normal force \bar{f}_n for the initial high-porosity packing (left column), the pre-compaction packing (middle column) and the post-compaction packing (right column)

match surprisingly well with experimental observations, in terms of fields of porosity and incremental strains, despite the quite simplified microstructure consisting of spherical particles. The global mechanical responses are qualitatively consistent with the experimental results, both featuring three distinct stages in stress–strain relation (especially the plateau stage and re-hardening stage) and close evolution of volumetric strain.

3. Extra information has been extracted from the multi-scale simulation to facilitate deeper understanding of compaction bands. The incremental normalized debonding number N^I presents a peak at the initiation

of compaction bands, maintains an almost constant value during the steady propagation of compaction bands in the plateau stage and gradually decreases to about half the value at the re-hardening stage. More than half of the interparticle bonds remain intact at the end of the plateau stage. The platen frictional resistance is generally small as compared to the confining pressure and deviatoric stress, and reaches its peaks at the beginning of both the plateau stage and the re-hardening stage.

4. RVE scale analyses demonstrate a steady propagation of the compaction-dominated localization at the plateau stage, followed by a gradual transition to

shear-dominated deformation at the re-hardening stage. The localized compaction of a RVE is accompanied by substantial debonding, grain rearrangements and collapse of macropores. The analyses based on local porosity suggest that the collapse of macropores contributes more to the induced porosity reduction and tends to transform the high-porosity packing to the pre-removal state. The force chain networks visualize the collapse of macropores and the evolution of contact-based anisotropy during the localized compaction.

Despite the good match of compaction band patterns observed in the multiscale simulations with experiments, some discrepancies in the mechanical responses are also found. Notably, the stress peak in the numerical simulation is followed by a sudden stress drop before the plateau stage which disagrees with the experimental data. This is possibly due to the simplification in preparing the high-porosity RVE, e.g., the adoption of spherical particles, the relatively simple interparticle contact model and the limited number of particles in the RVE. Moreover, the increasing rate of volumetric strain in the re-hardening stage is relatively smaller as compared to the experiment. Neglecting particle crushing in the multiscale simulation may have contributed to this difference, since it may become important during the re-hardening stage. Further work is required in order to better reproduce the mechanical responses while maintaining consistent failure patterns.

Acknowledgements The study has been financially supported by the National Natural Science Foundation of China under project 51679207 and the Research Grants Council of Hong Kong through GRF project 16210017, CRF project C6012-15G and TBRs project T22-603/15-N. Laboratoire 3SR is part of the LabEx Tec 21 (Investissements d’Avenir—Grant Agreement No. ANR-11-LABX-0030).

References

- Andò E (2013) Experimental investigation of microstructural changes in deforming granular media using X-ray tomography. PhD thesis, Université de Grenoble, Grenoble
- Andò E, Hall SA, Viggiani G, Desrues J, Bésuelle P (2012) Grain-scale experimental investigation of localised deformation in sand: a discrete particle tracking approach. *Acta Geotech* 7(1):1–13. <https://doi.org/10.1007/s11440-011-0151-6>
- Argilaga A, Desrues J, Pont SD, Combe G, Caillerie D (2018) FEM × DEM multiscale modeling: model performance enhancement from Newton strategy to element loop parallelization. *Int J Numer Methods Eng* 114(1):47–65. <https://doi.org/10.1002/nme.5732>
- Aydin A, Ahmadov R (2009) Bed-parallel compaction bands in aeolian sandstone: their identification, characterization and implications. *Tectonophysics* 479(3–4):277–284. <https://doi.org/10.1016/j.tecto.2009.08.033>
- Baud P, Klein E, Wong TF (2004) Compaction localization in porous sandstones: spatial evolution of damage and acoustic emission activity. *J Struct Geol* 26(4):603–624. <https://doi.org/10.1016/j.jsg.2003.09.002>
- Baud P, Exner U, Lommatzsch M, Reuschlé T, Tf Wong (2017) Mechanical behavior, failure mode, and transport properties in a porous carbonate. *J Geophys Res Solid Earth* 122(9):7363–7387. <https://doi.org/10.1002/2017JB014060>
- Baxevanis T, Papamichos E, Flornes O, Larsen I (2006) Compaction bands and induced permeability reduction in Tuffeau de Maastricht calcarenite. *Acta Geotech* 1(2):123–135. <https://doi.org/10.1007/s11440-006-0011-y>
- Bésuelle P, Rudnicki JW (2004) Localization: shear bands and compaction bands. *Int Geophys Ser* 89:219–322
- Challa V, Issen KA (2004) Conditions for compaction band formation in porous rock using a two-yield surface model. *J Eng Mech* 130(9):1089–1097. [https://doi.org/10.1061/\(ASCE\)0733-9399\(2004\)130:9\(1089\)](https://doi.org/10.1061/(ASCE)0733-9399(2004)130:9(1089))
- Charalampidou EM, Hall SA, Stanchits S, Viggiani G, Lewis H (2014) Shear-enhanced compaction band identification at the laboratory scale using acoustic and full-field methods. *Int J Rock Mech Min Sci* 67:240–252. <https://doi.org/10.1016/j.ijrmmms.2013.05.006>
- Cnudde V, Wirzen A, Masschaele B, Jacobs PJS (2009) Porosity and microstructure characterization of building stones and concretes. *Eng Geol* 103(3):76–83. <https://doi.org/10.1016/j.enggeo.2008.06.014>
- Collin F, Chambon R, Charlier R (2006) A finite element method for poro mechanical modelling of geotechnical problems using local second gradient models. *Int J Numer Methods Eng* 65(11):1749–1772. <https://doi.org/10.1002/nme.1515>
- Das A, Nguyen GD, Einav I (2011) Compaction bands due to grain crushing in porous rocks: a theoretical approach based on breakage mechanics. *J Geophys Res* 116:B08203. <https://doi.org/10.1029/2011JB008265>
- Das A, Nguyen GD, Einav I (2013) The propagation of compaction bands in porous rocks based on breakage mechanics. *J Geophys Res Solid Earth* 118(5):2049–2066. <https://doi.org/10.1002/jgrb.50193>
- Das A, Tengattini A, Nguyen GD, Viggiani G, Hall SA, Einav I (2014) A thermomechanical constitutive model for cemented granular materials with quantifiable internal variables. Part II—validation and localization analysis. *J Mech Phys Solids* 70(1):382–405. <https://doi.org/10.1016/j.jmps.2014.05.022>
- Dattola G, di Prisco C, Redaelli I, Utili S (2014) A distinct element method numerical investigation of compaction processes in highly porous cemented granular materials. *Int J Numer Anal Methods Geomech* 38(11):1101–1130. <https://doi.org/10.1002/nag.2241>
- Desrues J, Argilaga A, Dal Pont S, Combe G, Caillerie D, kein Nguyen T (2017) Restoring Mesh Independency in FEM–DEM Multi-scale modelling of strain localization using second gradient regularization. In: Papamichos E, Papanastasiou P, Pasternak E, Dyskin A (eds) *Bifurcation and degradation of geomaterials with engineering applications*. Springer series in geomechanics and geoengineering. Springer, Berlin, pp 453–457. 978-3-319-56397-8_57
- Desrues J, Argilaga A, Caillerie D, Combe G, Nguyen TK, Richefeu V, Pont SD (2019) From discrete to continuum modelling of boundary value problems in geomechanics: an integrated FEM–DEM approach. *Int J Numer Anal Methods Geomech* 43(5):919–955. <https://doi.org/10.1002/nag.2914>
- Fortin J, Stanchits S, Dresen G, Guéguen Y (2006) Acoustic emission and velocities associated with the formation of compaction bands in sandstone. *J Geophys Res* 111:B10203. <https://doi.org/10.1029/2005JB003854>

20. Fossen H, Bale A (2007) Deformation bands and their influence on fluid flow. *AAPG Bull* 91(12):1685–1700. <https://doi.org/10.1306/07300706146>
21. Fossen H, Schultz RA, Torabi A (2011) Conditions and implications for compaction band formation in the Navajo Sandstone, Utah. *J Struct Geol* 33(10):1477–1490. <https://doi.org/10.1016/j.jsg.2011.08.001>
22. Fossen H, Soliva R, Ballas G, Trzaskos B, Cavalcante C, Schultz RA (2017) A review of deformation bands in reservoir sandstones: geometries, mechanisms and distribution. *Geol Soc Lond Spec Publ* 459:9–33. <https://doi.org/10.1144/SP459.4>
23. Guo N, Zhao J (2013) The signature of shear-induced anisotropy in granular media. *Comput Geotech* 47:1–15. <https://doi.org/10.1016/j.compgeo.2012.07.002>
24. Guo N, Zhao J (2014) A coupled FEM/DEM approach for hierarchical multiscale modelling of granular media. *Int J Numer Methods Eng* 99(11):789–818. <https://doi.org/10.1002/nme.4702>
25. Guo N, Zhao J (2014) Local fluctuations and spatial correlations in granular flows under constant-volume quasistatic shear. *Phys Rev E* 89(4):042208. <https://doi.org/10.1103/PhysRevE.89.042208>
26. Guo N, Zhao J (2016) 3D multiscale modeling of strain localization in granular media. *Comput Geotech* 80:360–372. <https://doi.org/10.1016/j.compgeo.2016.01.020>
27. Guo N, Zhao J (2016) Multiscale insights into classical geomechanics problems. *Int J Numer Anal Methods Geomech* 40(3):367–390. <https://doi.org/10.1002/nag.2406>
28. Guo N, Zhao J (2016) Parallel hierarchical multiscale modelling of hydro-mechanical problems for saturated granular soils. *Comput Methods Appl Mech Eng* 305(9):768–785. <https://doi.org/10.1016/j.cma.2016.03.004>
29. Guo N, Zhao J, Sun W (2016) Multiscale analysis of shear failure of thick-walled hollow cylinder in dry sand. *Géotech Lett* 6(1):1–18. <https://doi.org/10.1680/jgele.15.00149>
30. Holcomb D, Rudnicki JW, Issen KA, Sternlof K (2007) Compaction localization in the Earth and the laboratory: state of the research and research directions. *Acta Geotech* 2(1):1–15. <https://doi.org/10.1007/s11440-007-0027-y>
31. Li X, Liang Y, Duan G, Schrefler B, Du Y (2014) A mixed finite element procedure of gradient Cosserat continuum for second-order computational homogenisation of granular materials. *Comput Mech* 54(5):1331–1356. <https://doi.org/10.1007/s00466-014-1062-9>
32. Li Z, Wang YH, Ma CH, Mok CMB (2017) Experimental characterization and 3D DEM simulation of bond breakages in artificially cemented sands with different bond strengths when subjected to triaxial shearing. *Acta Geotech* 12(5):987–1002. <https://doi.org/10.1007/s11440-017-0593-6>
33. Liu Y, Sun W, Yuan Z, Fish J (2016) A nonlocal multiscale discrete-continuum model for predicting mechanical behavior of granular materials. *Int J Numer Methods Eng* 106(2):129–160. <https://doi.org/10.1002/nme.5139>
34. Marketos G, Bolton M (2009) Compaction bands simulated in discrete element models. *J Struct Geol* 31(5):479–490. <https://doi.org/10.1016/j.jsg.2009.03.002>
35. Mollema PN, Antonellini MA (1996) Compaction bands: a structural analog for anti-mode I cracks in aeolian sandstone. *Tectonophysics* 267(1–4):209–228. [https://doi.org/10.1016/S0040-1951\(96\)00098-4](https://doi.org/10.1016/S0040-1951(96)00098-4)
36. Oka F, Kimoto S, Higo Y, Ohta H, Sanagawa T, Kodaka T (2011) An elasto-viscoplastic model for diatomaceous mudstone and numerical simulation of compaction bands. *Int J Numer Anal Methods Geomech* 35(2):244–263. <https://doi.org/10.1002/nag.987>
37. Olsson WA (1999) Theoretical and experimental investigation of compaction bands in porous rock. *J Geophys Res* 104(B4):7219–7228. <https://doi.org/10.1029/1998JB900120>
38. Olsson WA, Holcomb DJ (2000) Compaction localization in porous rock. *Geophys Res Lett* 27(21):3537–3540. <https://doi.org/10.1029/2000GL011723>
39. Olsson WA, Holcomb DJ, Rudnicki JW (2002) Compaction localization in porous sandstone: implications for reservoir mechanics. *Oil Gas Sci Technol* 57(5):591–599. <https://doi.org/10.2516/ogst:2002040>
40. Papazoglou A, Shahin G, Marinelli F, Dano C, Buscarnera G, Viggiani G (2017) Localized compaction in Tuffeau de Maastricht: experiments and modeling. In: *Bifurcation and degradation of geomaterials with engineering applications*. Springer series in geomechanics and geoenvironmental engineering. Springer, Cham, pp 481–488. https://doi.org/10.1007/978-3-319-56397-8_61
41. Papazoglou A, Bésuelle P, Dano C, Viggiani G (2019) Full 3D investigation of localized compaction in Tuffeau de Maastricht using X-ray computed tomography (**under review**)
42. Rescic S, Fratini F, Tiano P (2010) On-site evaluation of the ‘mechanical’ properties of Maastricht limestone and their relationship with the physical characteristics. *Geol Soc Lond Spec Publ* 331(1):203–208. <https://doi.org/10.1144/SP331.18>
43. Rudnicki JW (2004) Shear and compaction band formation on an elliptic yield cap. *J Geophys Res* 109:B03402. <https://doi.org/10.1029/2003JB002633>
44. Rudnicki JW, Rice JR (1975) Conditions for the localization of deformation in pressure-sensitive dilatant materials. *J Mech Phys Solids* 23(6):371–394. [https://doi.org/10.1016/0022-5096\(75\)90001-0](https://doi.org/10.1016/0022-5096(75)90001-0)
45. Schaa R, Gross L, du Plessis J (2016) PDE-based geophysical modelling using finite elements: examples from 3D resistivity and 2D magnetotellurics. *J Geophys Eng* 13(2):S59. <https://doi.org/10.1088/1742-2132/13/2/S59>
46. Shahin G, Desrues J, Pont SD, Combe G, Argilaga A (2016) A study of the influence of REV variability in double-scale FEM × DEM analysis. *Int J Numer Methods Eng* 107(10):882–900. <https://doi.org/10.1002/nme.5202>
47. Papazoglou A, Marinelli F, Buscarnera G (2019) Simulation of localized compaction in Tuffeau de Maastricht based on evidence from X-ray tomography. *Int J Rock Mech Min Sci* 121:104039. <https://doi.org/10.1016/j.ijrmms.2019.05.005>
48. Smilauer V, Catalano E, Chareyre B, Dorofeenko S, Duriez J, Dyck N, Elias J, Er B, Eulitz A, Gladky A, Jakob C, Kneib F, Kozicki J, Marzougui D, Maurin R, Modenesse C, Scholtes L, Sibille L, Stransky J, Sweijen T, Thoeni K, Yuan C (2015) Yade documentation, 2nd Ed. The Yade project. <https://doi.org/10.5281/zenodo.34073>
49. Tembe S, Baud P, Wong TF (2008) Stress conditions for the propagation of discrete compaction bands in porous sandstone. *J Geophys Res* 113:B09409. <https://doi.org/10.1029/2007JB005439>
50. Tengattini A, Das A, Nguyen GD, Viggiani G, Hall SA, Einav I (2014) A thermomechanical constitutive model for cemented granular materials with quantifiable internal variables. Part I—theory. *J Mech Phys Solids* 70(Supplement C):281–296. <https://doi.org/10.1016/j.jmps.2014.05.021>
51. Viggiani G, Andò E, Takano D, Santamarina JC (2015) Laboratory X-ray tomography: a valuable experimental tool for revealing processes in soils. *Geotech Test J* 38(1):61–71. <https://doi.org/10.1520/GTJ20140060>
52. Wang B, Chen Y, Wong TF (2008) A discrete element model for the development of compaction localization in granular rock. *J Geophys Res* 113:B03202. <https://doi.org/10.1029/2006JB004501>

53. Wang K, Sun W (2016) A semi-implicit discrete-continuum coupling method for porous media based on the effective stress principle at finite strain. *Comput Methods Appl Mech Eng* 304:546–583. <https://doi.org/10.1016/j.cma.2016.02.020>
54. Wong TF, Baud P (2012) The brittle-ductile transition in porous rock: a review. *J Struct Geol* 44:25–53. <https://doi.org/10.1016/j.jsg.2012.07.010>
55. Wong TF, David C, Zhu W (1997) The transition from brittle faulting to cataclastic flow in porous sandstones: mechanical deformation. *J Geophys Res* 102(B2):3009–3025. <https://doi.org/10.1029/96JB03281>
56. Wong TF, Baud P, Klein E (2001) Localized failure modes in a compactant porous rock. *Geophys Res Lett* 28(13):2521–2524. <https://doi.org/10.1029/2001GL012960>
57. Wu H, Zhao J, Guo N (2015) Multiscale modelling of compaction bands in highly porous sandstone. In: *The first international conference on geo-energy and geo-environment*, HKUST, Hong Kong, p 125
58. Wu H, Guo N, Zhao J (2017) Borehole instabilities in granular rocks revisited: a multiscale perspective. In: Papamichos E, Papanastasiou P, Pasternak E, Dyskin A (eds) *Bifurcation and degradation of geomaterials with engineering applications*. Springer series in geomechanics and geoenvironment. Springer, Cham, pp 433–439. https://doi.org/10.1007/978-3-319-56397-8_54
59. Wu H, Guo N, Zhao J (2018) Multiscale modeling and analysis of compaction bands in high-porosity sandstones. *Acta Geotech* 13(3):575–599. <https://doi.org/10.1007/s11440-017-0560-2>
60. Wu H, Zhao J, Guo N (2018) Multiscale insights into borehole instabilities in high-porosity sandstones. *J Geophys Res Solid Earth* 123(5):3450–3473. <https://doi.org/10.1029/2017JB015366>
61. Wu H, Zhao J, Guo N (2019) Multiscale modeling of compaction bands in saturated high-porosity sandstones. *Eng Geol* 261:105282. <https://doi.org/10.1016/j.enggeo.2019.105282>
62. Zhao J, Guo N (2015) The interplay between anisotropy and strain localisation in granular soils: a multiscale insight. *Géotechnique* 65(8):642–656. <https://doi.org/10.1680/geot.14.P.184>
63. Zhao S, Zhou X (2017) Effects of particle asphericity on the macro- and micro-mechanical behaviors of granular assemblies. *Granul Matter* 19(2):38. <https://doi.org/10.1007/s10035-017-0725-6>

Publisher's Note Springer Nature remains neutral with regard to jurisdictional claims in published maps and institutional affiliations.